

Design and Characterization of *W*-Band Silicon Micromachined High-Power and High-Speed Photoconductive Evanescent-Mode Waveguide Single and Double Throw Switches

Eric T. Der¹, Graduate Student Member, IEEE, Thomas R. Jones², Member, IEEE, Alden Fisher³, Member, IEEE, Kambiz Moez⁴, Senior Member, IEEE, Douglas W. Barlage⁵, Senior Member, IEEE, and Dimitrios Peroulis⁶, Fellow, IEEE

Abstract—This article details the principle of operation, design process, and characterization of *W*-band silicon micromachined evanescent-mode (EVA) waveguide switches. This work includes a detailed analysis of the ON-state response of EVA waveguide switches as well as the design of transitions to standard waveguide connector feeds. The first ever switching speed and power handling characterization of silicon micromachined EVA waveguide switches is also presented. Photogenerated plasma in silicon posts placed inside an EVA channel results in large impedance mismatch, allowing very high isolation to be achieved in the switch's OFF-state with low optical power. In the ON-state, the unexcited silicon posts behave as shunt capacitors, allowing signal propagation through the switch in the form of a coupled resonator bandpass filter response. The design of both two-pole and three-pole filter responses in single pole single throw (SPST) and single pole double throw (SPDT) switch configurations is detailed in this article. The fabricated two-pole SPST switch achieves a 30-dB isolation with just 178 mW of optical excitation. For the three-pole SPST switch, only 111 mW is required. The extracted insertion loss (IL) of the two-pole and three-pole switching elements in SPDT configurations is just 0.16 and 0.32 dB, respectively. Furthermore, experiments presented in this article show that $4\text{-}\mu\text{s}$ switching speeds are realized by this technology, and that the switching elements are able to handle at least +32 dBm of continuous power at 85 GHz.

Index Terms—Evanescent-mode (EVA), 5G, millimeter-wave (mmWave), photoconductive switch, silicon micromachining, 6G, waveguide.

Manuscript received 11 July 2023; revised 19 September 2023; accepted 13 October 2023. Date of publication 9 November 2023; date of current version 10 January 2024. This work was supported in part by the Canadian Department of National Defense, in part by CMC Microsystems, and in part by Jones Microwave Inc. This article is an expanded paper from the IEEE MTT-S Int. Microwave Symposium held on June 11–16, 2023 in San Diego, USA [DOI: 10.1109/LMWT.2023.3268947]. (Corresponding author: Eric T. Der.)

Eric T. Der, Kambiz Moez, and Douglas W. Barlage are with the Department of Electrical and Computer Engineering, University of Alberta, Edmonton, AB T6G 1H9, Canada (e-mail: der@ualberta.ca; kambiz@ualberta.ca; barlage@ualberta.ca).

Thomas R. Jones, Alden Fisher, and Dimitrios Peroulis are with the Elmore Family School of Electrical and Computer Engineering, Purdue University, West Lafayette, IN 47907 USA (e-mail: jone2006@purdue.edu; fishe128@purdue.edu; dperouli@purdue.edu).

Color versions of one or more figures in this article are available at <https://doi.org/10.1109/TMTT.2023.3328483>.

Digital Object Identifier 10.1109/TMTT.2023.3328483

I. INTRODUCTION

OVER the past decade, the deployment of the fifth generation of wireless communication systems (5G) has spearheaded the development of millimeter-wave (mmWave) technologies in order to meet the growing demand for connectivity and higher data transfer rates. These demands can be met due to the relative abundance of spectra available in the mmWave domain above 30 GHz [1]. Beyond the speed and latency benefits of mmWaves, there are additional benefits of reduced physical footprints of communication devices as the design frequency increases. Moving forward, major players in the telecommunication industry have already proposed a sixth generation of wireless communications (6G) where development beyond 100 GHz has already begun [2], [3], [4]. Additionally, radar technology in the *W*-band has been developed over the past few decades for defense and aviation applications [5], [6]. Recent literature also proposed developments into the *D*-band for 6G communications and automotive radar applications [7], [8], demonstrating a need for a better understanding of mmWave and sub-THz technologies.

Although the benefits of mmWave to the future of wireless communications are clear, there remain significant gaps in available technology at these frequencies. In order to achieve greater range and improved link margins as well as to compensate for higher atmospheric attenuation, mmWave radio transmitters require higher output powers to maintain an adequate signal-to-noise ratio (SNR) [9]. According to the Friis equation, this can be achieved by either using high gain antennas (i.e., antenna arrays), or by increasing radio frequency (RF) power at the transmitter [10]. Investigations between 71 and 86 GHz (*E*-band) have shown 6-Gb/s data rates over 36 km with transmitter powers of 0.7 W [11], and is expected to be even higher in the *W*-band (75–110 GHz). One significant challenge with increased power is the capability of the transceiver front-end system to handle it. At mmWave frequencies, front-ends typically use waveguides due to their high power handling and low insertion loss (IL). However, many of these solutions are manufactured through traditional

metal-machining, limiting their ability to be mass-produced and are generally difficult to integrate with planar microwave technologies.

As fundamental components of transceiver front-ends, RF switches enable functionality including reconfiguration [12], antenna transmit–receive switching or beamswitching [13], [14], [15], or band and channel selection in multiband systems. While a variety of mmWave switch technologies using electromechanical rotors and p-i-n diodes currently exist, there are generally major trade-offs among power handling, size, and speed [16], [17], [18], [19], [20]. Electromechanical waveguide switches offer the highest continuous wave (CW) power handling. However, they have switching speeds on the order of several milliseconds which may significantly increase the latency of communication systems [17]. Additionally, the use of electromechanical rotors requires large, heavy packaging and is less reliable than solid-state components, having a service life of around 250 000 cycles [18]. p-i-n diode switches, on the other hand, offer switching speeds on the order of nanoseconds [19], and have exceptional power handling at lower RF bands [21]. However, at mmWave frequencies, p-i-n diodes lose their CW power handling, suffer large ILs, poor signal isolation, and have low linearity [19].

Researchers have also explored the use of the photoconductive effect in semiconductors for a variety of integrated microwave engineering applications including switches [22], [23], variable attenuators [24], and tunable filters [25]. Photoconductive switches have the benefit of relatively high power handling and excellent linearity [26] while also offering fast switching speeds and low ILs with the right choice of material and optical power [27], [28]. Moreover, photoconductive switches have the additional benefit of bias networks completely isolated from the RF path, further improving IL and linearity. Within waveguide structures, photoexcitation can be used to alter the properties of high resistivity silicon (HR-Si) posts, changing them from a dielectric to a conductor. When the light source is switched off, the dielectric properties of the posts are restored, effectively allowing microwave signals to be dynamically redirected within the waveguide channel [29], [30], [31]. As will be determined from the studies in this article, photoconductive silicon waveguide switches offer an excellent compromise between the switching speed of p-i-n diode-based solutions and the high power handling capabilities of electromechanical waveguide switches while also operating at mmWave frequencies. These light-activated switches will open up entirely new use cases for reconfigurable and multifunctional mmWave technology by offering high-speed and high power handling with low ON-state IL and high OFF-state isolation simultaneously within the same device.

The advantages of photoconductive switch technology in both planar and waveguide platforms have been thoroughly documented by Fisher et al. [27], [32], [33], [34], Jones et al. [29], [30], and Der et al. [31]. In [27], a dc to 7-GHz reflective series switch constructed in a microstrip platform was shown to be able to handle 35 W of RF power, with an absorptive single-pole double throw (SPDT) switch implementation demonstrated in [33]. More recently in [34], it was shown that up to 100 W of RF power can be handled without degradation

in loss or isolation, while also demonstrating hot switching up to 30 W. The first ever dc to 110-GHz photoconductive switch in coplanar-waveguide (CPW) technology was also demonstrated in [32].

While integrating mechanically tuned posts within waveguide switches and filters has been demonstrated [35], Jones et al. [29] presented the first waveguide switch incorporating photoconductive silicon posts within the waveguide channel as the switching element fabricated using silicon bulk micromachining at mmWave frequencies. Silicon bulk micromachining has the advantages of relatively simple planar integration with very tight feature tolerances on the order of a few micrometers, and has been demonstrated to successfully fabricate waveguide structures that operate up to sub-THz frequencies [36]. Furthermore, silicon micromachining allows the waveguide channel and photoconductive silicon switch posts to be fabricated monolithically with the same process [29]. In [30], silicon micromachined photoconductive waveguide switch technology was further developed by demonstrating that the optical power requirement for achieving a high isolation can be significantly reduced by fabricating a switch topology with two silicon posts inside an evanescent-mode (EVA) waveguide channel.

This article is an extension of [31], which demonstrated preliminary results of the first ever integration of silicon micromachined photoconductive EVA waveguide switches in an SPDT configuration. The work also replaced a planar transmission line feed in favor of a standard waveguide connectorized design and provided the baseline small-signal S-parameter performance. In this article, we have expanded on this work by including a detailed theoretical analysis on photoconductive EVA waveguide channel and switch design, the design procedure for a standard to reduced-height waveguide transition, the first demonstration of both single pole single throw (SPST) and SPDT switch designs with three posts to further reduce the optical power requirement, and the first ever characterization of the switching speed and power handling of this waveguide switch technology within the W-band.

This article is structured as follows. First, the fundamental operating principles, theory, and design of photoconductive EVA waveguide switches are presented; namely, the photoconductive effect along with filter theory using coupled resonators. In Section III, the fundamental design considerations, limitations, trade-offs, and simulated results of photoconductive EVA waveguide switches are discussed. Section IV discusses the design considerations for practical implementations of the proposed switches, with the assembly of the fabricated devices presented in Section V. Finally, in Section VI, the experimental setup and characterization results of the fabricated devices, including switching speed and power handling, are presented and discussed.

II. PRINCIPLE OF OPERATION

The fundamental operating principle behind the proposed switch is a combination of the photoconductive effect with EVA waveguide theory. The conductivity of a silicon post can be controlled by the magnitude of optical excitation. When

silicon posts are placed inside an EVA waveguide channel in their dielectric state, a bandpass filter response can be established. In their conductive state, the combination of a waveguide in its cutoff state and a low-impedance shunt from the posts yields very high impedance mismatches, allowing very high switch isolations to be achieved with low-intensity optical excitation [30].

A. Photoconductive Effect

Conductivity can be induced in a semiconductor through excitation with light at a photon energy greater than the bandgap of the semiconductor, generating electron hole pairs inside the material. HR-Si is a good candidate for the switching element due to its ability to act as a low-loss dielectric at the mmWave band in the absence of photoexcitation. Furthermore, its relatively low bandgap offers an abundance of high-power optics solutions for inducing high conductivity. The dc conductivity of silicon can be computed as follows [29], [37]:

$$\sigma_{dc} = q(\mu_p + \mu_n)n' \quad (1)$$

where q is the elementary charge, n' is the excess carrier concentration (assumed to be uniform in the material), and μ_n and μ_p are the carrier mobilities of electrons and holes, respectively. The carrier mobilities of silicon, with n' in units of cm^{-3} and μ_n and μ_p in units of $\text{cm}^2\text{V}^{-1}\text{s}^{-1}$, can be calculated as follows [29], [38]:

$$\mu_n = \frac{1318}{1 + \left(\frac{n'}{1 \times 10^{17}}\right)^{0.85}} + 92 \quad (2)$$

$$\mu_p = \frac{420}{1 + \left(\frac{n'}{1.6 \times 10^{17}}\right)^{0.7}} + 50. \quad (3)$$

With this, (1) can be written to be entirely dependent on the excess carrier concentration n' which can be computed as a function of photoexcitation as follows [29], [37]:

$$n' = \frac{P_0/h\nu}{\alpha H^2} \tau (1 - R)(1 - e^{-\alpha H}) \quad (4)$$

where P_0 is the incident light intensity, R and α are, respectively, the reflection and absorption coefficients of the material—which can be calculated from the real and imaginary components of the refractive index— τ the carrier lifetime, and H the height of the semiconducting material under excitation. It can be seen from (1)–(4) that the conductivity of the silicon switching elements increases with optical power. It was previously shown in [29] that HR-Si posts extending from top to bottom of a rectangular waveguide channel at its center can be used to switch it ON/OFF to incident RF signals. When excited with photons above the bandgap energy of silicon ($E_g = 1.12$ eV [37]), the HR-Si posts enter their conductive state and shorts the TE_{10} mode of the waveguide channel where the electric field is strongest (at the center of the channel). When no light is present, the HR-Si acts as a low-loss dielectric and will allow RF propagation through the waveguide.

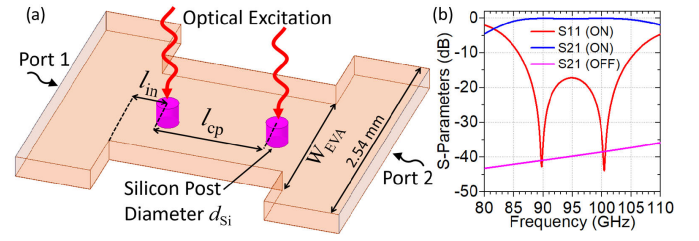


Fig. 1. (a) 3-D model of a simple silicon photoconductive EVA waveguide switch. W_{EVA} represents the width of the EVA channel, l_{cp} the coupling distance between the silicon posts (center-to-center), and l_{in} the input coupling length. Optical fibers can be used to switch the HR-Si posts inside the waveguide channel between its dielectric and conductive states. The height of the waveguide cavity is $200 \mu\text{m}$. The nominal values of l_{in} , l_{cp} , and W_{EVA} are 0.3 , 1.02 , and 1.5 mm, respectively. The nominal silicon post diameter (d_{Si}) is 0.2 mm. (b) Simulation of the 3-D models using the nominal dimensions.

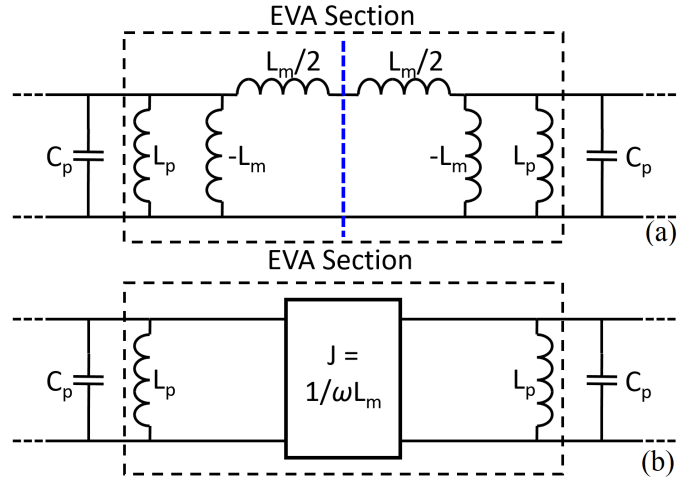


Fig. 2. Equivalent lumped circuit model of an EVA waveguide section loaded with two dielectric posts at each end. (a) Transmission line section of an EVA guide can be represented by a π -network of inductors whose values vary by the length and width of the section. (b) With the dielectric posts that create a capacitance C_p , the evanescent guide effectively forms a two-pole J-inverter-coupled bandpass filter response where $J = 1/\omega L_m$.

B. Evanescent-Mode Waveguide Coupled Resonators

A 3-D model of a two-pole silicon photoconductive EVA waveguide switch is illustrated in Fig. 1. In the OFF-state of the switch, the silicon posts are excited with 915-nm light from the optical fibers; the posts become conductive due to the photoconductive effect. The now conductive posts at the center of the channel short the fundamental TE_{10} mode where the electric field is the strongest. Coupled with the fact that the narrow channel is already operating below cutoff, very high OFF-state isolation can be achieved with this design.

In rectangular waveguides, it is known that below the cutoff frequency of its fundamental TE_{10} mode, the waveguide—now in EVA—begins to behave as an inductive component in a π -configuration [39], [40] as shown in Fig. 2. The inductances are defined by

$$L_m = X_0/\omega \cdot \sinh \gamma l \quad (5)$$

$$L_p = X_0/\omega \cdot \tanh \gamma l/2 \quad (6)$$

where l is the length of EVA channel and [39]

$$X_0 = \frac{120\pi b}{W_{\text{EVA}} \sqrt{\left(\frac{\lambda}{2W_{\text{EVA}}}\right)^2 - 1}} \quad (7)$$

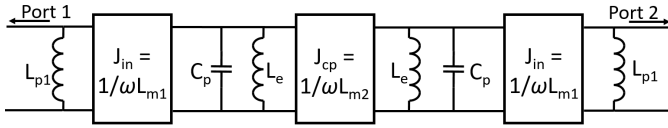


Fig. 3. Equivalent J-inverter circuit model of the proposed two-pole photoconductive EVA waveguide switch.

$$\gamma = \frac{2\pi}{\lambda} \sqrt{\left(\frac{\lambda}{2W_{\text{EVA}}}\right)^2 - 1}. \quad (8)$$

The height of the channel is represented by b , λ represents the wavelength, and W_{EVA} the width of the EVA channel.

EVA waveguides do not normally allow propagation of RF signals or power. However, in the ON-state of this switch, the loading of the channel with dielectric posts—which behave as shunt capacitors—in unison with the π -connected inductors of the EVA waveguide lumped model will effectively form a filter response with J-inverters where $J = 1/\omega L_m$. Fig. 2 shows a general filter model with two resonators (filter poles) coupled with an inductive π -network J-inverter.

In even-mode excitation, i.e., when a magnetic wall (open circuit) is inserted at the blue dotted reference plane in Fig. 2, the resulting resonant frequency can be calculated using the method detailed in [41] as

$$f_m = \frac{1}{2\pi \sqrt{\frac{L_m L_p}{L_m - L_p} C_p}}. \quad (9)$$

Likewise, in odd-mode excitation, i.e., when an electric wall (short circuit) is inserted instead, the resonant frequency is computed with

$$f_e = \frac{1}{2\pi \sqrt{\frac{L_m L_p}{L_m + L_p} C_p}}. \quad (10)$$

As the inverter inductance L_m approaches a very large value in (9) and (10), both f_m and f_e converge to $1/2\pi(LC_p)^{1/2}$, the natural resonant frequency of a single uncoupled resonator. Conversely, as L_m decreases, f_m and f_e will diverge indicating an increase in coupling between the resonators. Since L_m is proportional to $\sinh \gamma l$, it can be inferred that the interresonator coupling (k) which can be extracted using $k = (f_e^2 - f_m^2)/(f_e^2 + f_m^2)$ increases with the decrease in length of the EVA channel in between two dielectric posts. Additionally, it can be seen from (9) and (10) that f_e is a higher frequency than f_m which is indicative of magnetic coupling between the dielectric posts [41].

In order to couple energy to the bandpass filter response in a practical switch's ON-state, a short length of EVA waveguide (l_{in}) needs to run between the waveguide feed and the first resonating post as shown in Fig. 1. The final equivalent J-inverter circuit is shown in Fig. 3. The resulting inductive components from the three EVA sections are defined as follows [39]:

$$\omega L_{m(n)} = \sinh \gamma l_n \quad (11)$$

$$\frac{1}{\omega L_{p(n)}} = \coth \gamma l_n \quad (12)$$

$$\frac{1}{\omega L_e} = \frac{1}{\omega L_{p1}} + \frac{1}{\omega L_{p2}} = \coth \gamma l_1 + \coth \gamma l_2. \quad (13)$$

For the distance between posts $l_2 = l_{\text{cp}}$ [39]

$$\sinh \gamma l_2 = \frac{\delta \sqrt{g_1 g_2}}{\text{FBW}(\coth \gamma l_1 + \coth \gamma l_2)}. \quad (14)$$

For the input coupling length $l_1 = l_{\text{in}}$ [39]

$$\sinh \gamma l_1 = \sqrt{\frac{\delta g_1 R'}{\text{FBW}(\coth \gamma l_1 + \coth \gamma l_2)}} \quad (15)$$

where g_1 and g_2 are polynomial coefficients for filter prototypes (Chebyshev, Butterworth, etc.), R' is the feed waveguide impedance, and [39]

$$\delta = \frac{2}{1 + \frac{1}{1 - \left(\frac{2W_{\text{EVA}}}{\lambda_0}\right)^2}}. \quad (16)$$

III. LIMITATIONS AND TRADE-OFFS

The dimensions of the EVA channel, input coupling length, and coupling distance between posts all have performance trade-offs in the proposed switches. In [29], two EVA waveguide switch designs were presented: one where low ON-state IL was prioritized while sacrificing OFF-state isolation, and another where OFF-state isolation was prioritized while having higher ON-state IL. In this section, an in-depth study of the engineering trade-offs for the two-pole switch dimensions (l_{in} , l_{cp} , d_{Si} , and W_{EVA} in Fig. 1) is presented. All studies use a silicon conductivity of 0.1 S/m and sputtered copper conductivity of 2.3×10^7 S/m.

A. EVA Channel Width and Silicon Post Diameter

A parametric study of the EVA channel width (W_{EVA}) is shown in Fig. 4. The loss of the structure can be computed from $\text{Loss (dB)} = -10 \log(1 - \text{Loss})$, where $\text{Loss} = 1 - |S_{11}|^2 - |S_{21}|^2$ [42]. Fig. 4(a) demonstrates that as W_{EVA} increases, the switch has lower loss in its ON-state, but becomes more absorptive (lossy) in the OFF-state. The more W_{EVA} is decreased, the closer the OFF-state of the switch approaches an ideal short-circuit, as shown in Fig. 4(b).

From (6)–(8), it can be seen that the shunt inductances (l_p) will decrease with narrower EVA channels (W_{EVA}). This will result in an upshift in operating frequency. Furthermore, according to (8) and (14), the fractional bandwidth (FBW) of the switch will be reduced as W_{EVA} decreases. In the OFF-state of the switch, a narrower W_{EVA} yields higher isolation due to a greater impedance mismatch at a given optical power with the EVA waveguide region further in cutoff [30].

To increase the FBW of an EVA waveguide switch, W_{EVA} must increase, but doing so will cause a downshift in operating frequency unless the silicon post diameter (capacitive loading) is decreased to compensate. From Fig. 5, decreasing the post diameter generally decreases ON-state loss, but also decreases the reflectivity of the OFF-state. Therefore, it can be concluded that there is a fundamental trade-off between the ON-state IL and FBW with the OFF-state reflectivity and isolation of the switch.

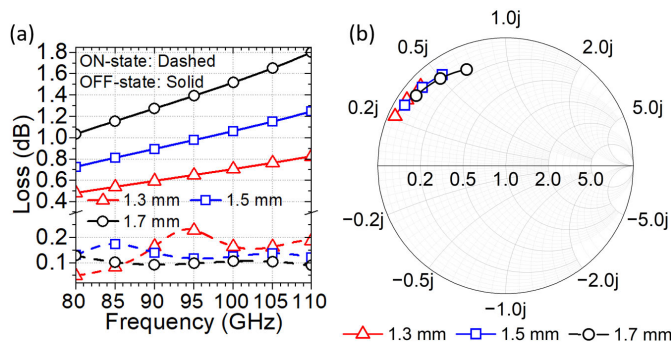


Fig. 4. Parametric study of the effect of W_{EVA} on switch performance. (a) Loss of the switch in the ON-state and OFF-state. (b) Input impedance of the switch in the OFF-state.

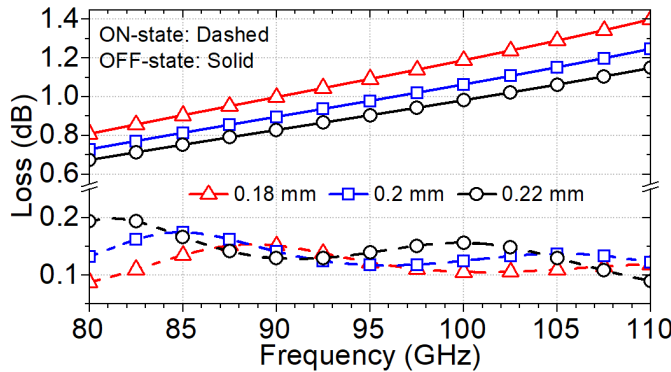


Fig. 5. Parametric study of the effect of the silicon post diameter (d_{si}) on switch loss.

B. Input Coupling

A parametric study of the input coupling distance, l_{in} (between the start of the EVA waveguide and the center of the first post), is shown in Fig. 6. In Fig. 6(a), the power dissipation in the ON-state increases with l_{in} , but decreases in the OFF-state as l_{in} is increased. In Fig. 6(b), while decreasing l_{in} makes the OFF-state of the switch less inductive, it also makes it less reflective, as the resistive post is moved closer to the input port of the switch.

A plot of the external quality factor (Q_e) versus l_{in} is shown in Fig. 7, obtained from detuning the post adjacent to port 2 in Fig. 1 and extracting Q_e using the method in [43]. Clearly, increases in l_{in} result in an increase in Q_e corresponding to a decrease in input coupling. From (15), an increase in $l_1 = l_{in}$ will result in a decrease in resonator FBW due to a reduction in loading from the input ports.

C. Interresonator Coupling

A parametric study of the distance between two resonating posts (l_{cp}) is shown in Fig. 8. By decreasing the distance between the posts, the power dissipated by the switch is reduced in both the ON-state and OFF-state. Note that a Smith chart was not shown for this study as it was found that there was very little variation in the OFF-state input impedance across different l_{cp} since most of the power is already reflected by the first post of the incident signal encounters. From (14), increasing $l_2 = l_{cp}$ will decrease the FBW which is consistent with the phenomena observed in (9) and (10) where f_e and f_m

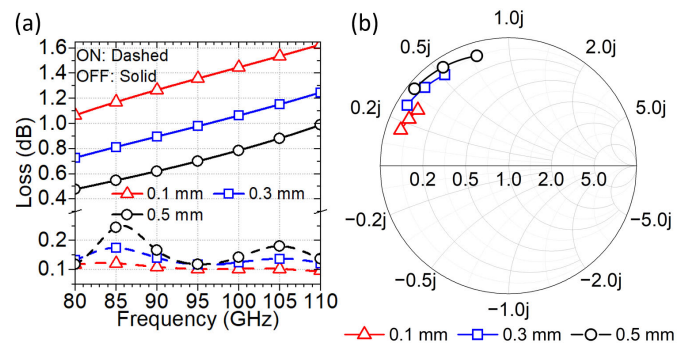


Fig. 6. Parametric study of the effect of l_{in} on switch performance. (a) Loss of the switch in the ON-state and OFF-state. (b) Input impedance of the switch in the OFF-state.

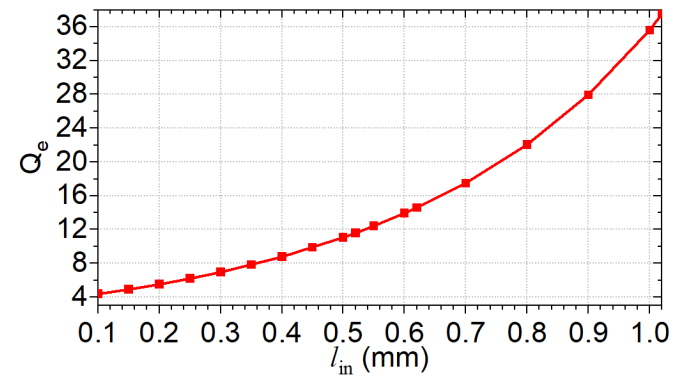


Fig. 7. Plot of the effect of l_{in} on the external quality factor (Q_e).

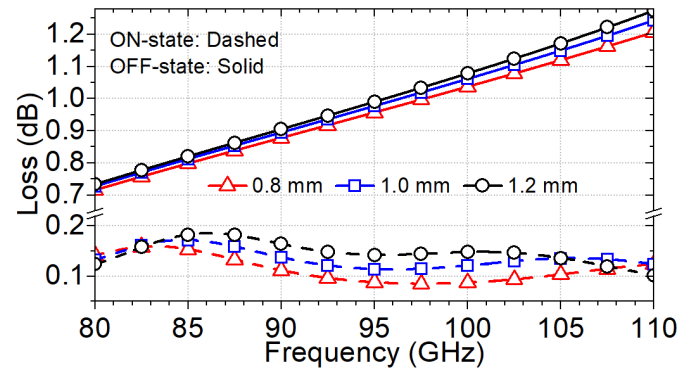


Fig. 8. Parametric study of the effect of l_{cp} on the ON- and OFF-state loss of the switch.

converge with an increased l_{cp} . Fig. 9 demonstrates that this increase in l_{cp} corresponds to a decrease in the interresonator coupling between the posts, which is also consistent with observations from (9), (10), and (14).

Therefore, in order to increase FBW, the coupling between posts should be increased. However, the input coupling must also be increased in order to reduce the ripple that will be introduced in between f_e and f_m as they move further apart. Based on the studies in Sections III-B and III-C, it is once again observed that the proposed switch has fundamental trade-offs between ON-state loss and FBW with OFF-state reflectivity and isolation. The switch's FBW is fundamentally limited by how much isolation is desired in the design.

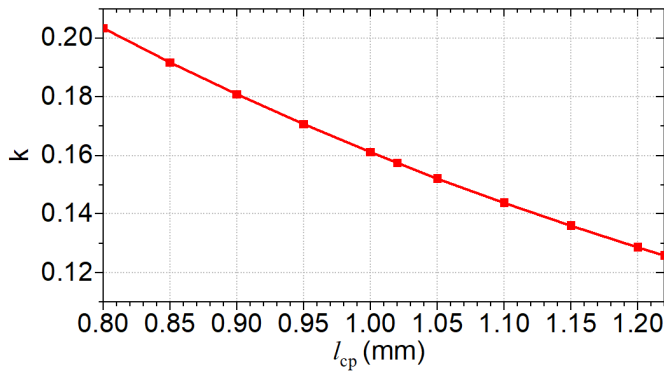


Fig. 9. Plot of the effect of l_{cp} on the coupling coefficient (k).

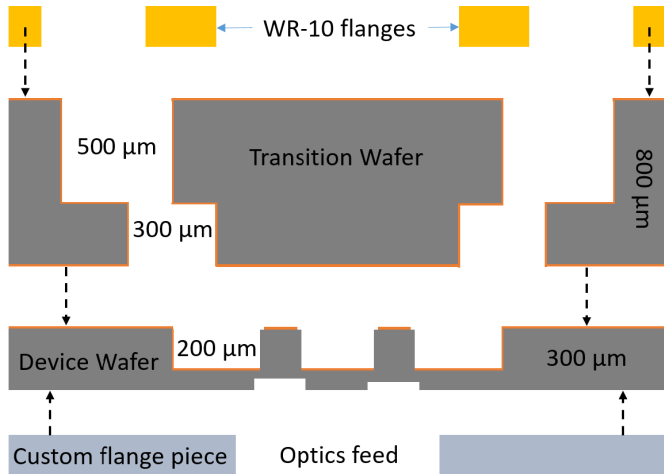


Fig. 10. Exploded longitudinal cross section of a silicon micromachined EVA waveguide switch. A 200- μm cavity is etched into a 300- μm HR-Si wafer to form the EVA channel and posts. Two cavities (500 and 300 μm deep) are etched in an 800- μm silicon wafer to form an E -plane bend and impedance taper that matches the 200- μm -device waveguide to standard WR-10 waveguide feeds. The device and transition wafers are sandwiched between WR-10 flange connectors and a custom laser cut sheet of stainless steel.

IV. DESIGN

With the proposed switches’ principle of operation and fundamental trade-offs and limitations established, we will now discuss the practical implementation of the device as well as the design of an SPDT version. Fig. 10 depicts the longitudinal cross section of the two-pole SPST switch implementation proposed in this section. The switch channel and posts are formed by etching a 200- μm cavity into a 300- μm 10-k Ω -cm HR-Si wafer. This device wafer is then sandwiched with an 800- μm Si transition wafer—with cavities etched on both sides—which serves both as an E -plane bend and impedance taper [36] between standard W -band WR-10 waveguide connectors and the 200- μm reduced height waveguides. The WR-10 flange connectors can be placed with an offset from the first transition cavity to allow for an extra degree of freedom when designing the impedance taper. 50- μm -deep holes are etched on the backside of the device wafer to allow for optical fibers controlling the two states of the photoconductive switch to be fed into each silicon post.

The close-up side view of the stacked-wafer E -plane bend used to feed the devices proposed in this article is presented in Fig. 11 along with 3-D models in Figs. 12 and 13.

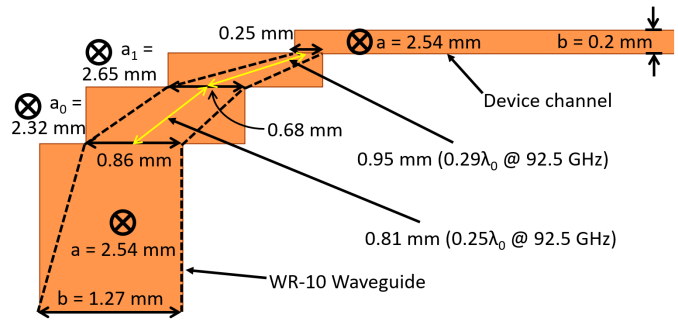


Fig. 11. Side view of the E -plane bend used to feed the proposed SPST switches. The bend also acts as an impedance taper to match a WR-10 waveguide to the proposed devices which have a reduced height of 0.2 mm. The yellow arrows show the distance between the centers of the openings between each step.

The impedance taper can be designed with the following procedure using a full-wave EM simulator.

- 1) Start with two decreasing step heights that are smaller than the standard waveguide height ($b = 1.27$ mm), but greater than the height of the device channel (0.2 mm). In this design, the step closer to the standard flange is 500 μm thick and the next step is 300 μm . For a single transition wafer implementation, such as for this work, the steps must add up to the total thickness of the wafer (800 μm).
- 2) Offset each waveguide step and the device (s_0 , s_1 , and s_2) and adjust the longitudinal length of each step (b_0 and b_1) such that the coupling apertures decrease in size with each successive step. To start, the distances between the center of each aperture should be approximately a quarter-wavelength at midband. For the W -band, the midband of 92.5 GHz has a $\lambda/4$ of 0.81 mm as shown by the yellow lines in Fig. 11.
- 3) If there is a very narrow or no observable passband in the simulated response, the change in step thickness is most likely causing significant impedance mismatches between steps. Repeat steps 1 and 2 with new step heights.
- 4) Fine tune the transverse widths (a_0 and a_1), offsets, and lengths of the two steps until the desired return loss (RL) response is achieved.

The 3-D model, simulation, and measured result of the transition are shown in Fig. 12. The length of line (8.15 mm) on the device wafer is the minimum length such that two standard WR-10 UG-387 waveguide connectors can fit on the fabricated design. This direct connection of the two transitions (i.e., a thru line) has a simulated and measured peak IL of 0.36 and 1.16 dB, respectively.

A. SPST EVA Switches With E -Plane Bend Transitions

The proposed switch’s channel is embedded inside a 300- μm wafer. To create a functional component, we must now consider how to interface with the device. In [29] and [30], transitions to CPW were developed for a similar device. While the transition is useful for characterization purposes using ground-signal-ground probes, it is not suitable for use in

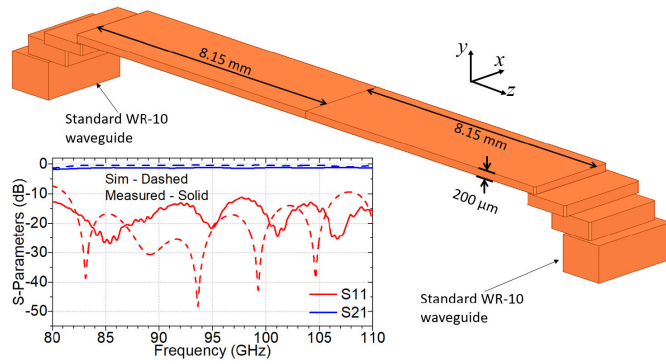


Fig. 12. 3-D model, simulation, and measured results of the E -plane bend transition with a waveguide thru line. The total length of the thru line is the combined length of the transitions feeding the two ports of the devices shown in Figs. 13 and 14.

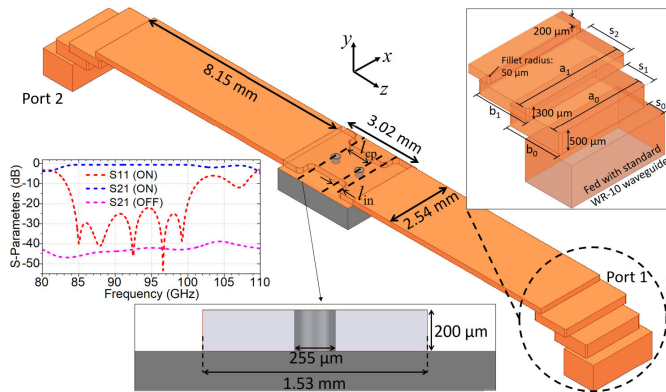


Fig. 13. 3-D model of the proposed two-pole photoconductive EVA switch fed with E -plane bend transitions to standard WR-10 waveguides. Note that the top silicon layer has been rendered transparent to allow visibility inside the structure. The widths of the transition steps a_0 and a_1 are 2.32 and 2.65 mm, respectively, the length of the transition steps b_0 and b_1 are 1.41 and 1.37 mm, respectively, and step offsets s_0 , s_1 , and s_2 are 0.41, 0.73, and 1.12 mm. The distance between the two posts l_{cp} is 1.02 mm, and the input coupling length l_{in} is 0.3 mm. From simulation, it can be seen that a 20-dB RL can be achieved spanning 85–100 GHz.

practical systems since planar transmission lines have poorer power handling in the W -band. To fully maximize the power handling of this waveguide switch technology at the W -band and beyond, it is prudent that the entire system itself be fed, interconnected, and connectorized purely with waveguide structures. In this design, the switches are fed with standard WR-10 waveguides. Fig. 13 depicts a two-pole EVA switch with an E -plane bend. Note that the corners of each transition layer are rounded with a fillet radius of $50 \mu\text{m}$ to improve the power handling of the device. Likewise, the corners at the interface between the 2.54-mm feed channel and 1.53-mm EVA channel have been rounded with a fillet radius of $150 \mu\text{m}$. In Fig. 13 it can be seen that an RL greater than 20 dB can be achieved across the entire 85–100-GHz design band with a total IL less than 0.6 dB. Furthermore, a minimum OFF-state isolation of 41.5 dB can be achieved in the design band.

An EVA waveguide is normally in cutoff when no resonant structures are coupled inside the cavity and propagating fields decay exponentially since the propagation constant (β) becomes imaginary [10]. It can therefore be inferred that by increasing the length of the EVA channel, the OFF-state

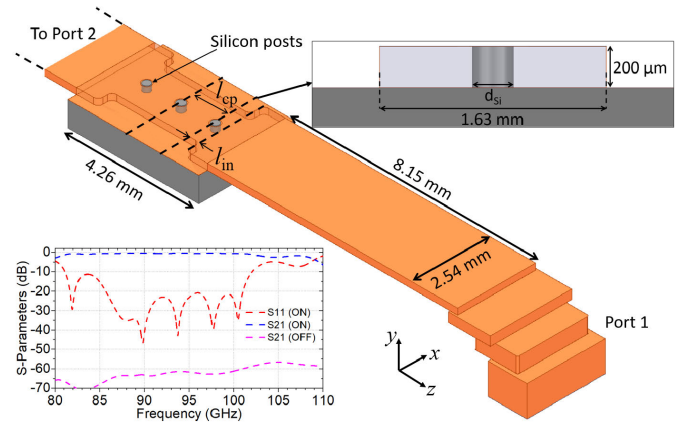


Fig. 14. 3-D model and simulation results of the proposed three-pole photoconductive EVA switch with E -bend transitions to WR-10 waveguides. Note that the top silicon layer has been rendered transparent to allow visibility inside the structure. The E -bend transition dimensions are identical to those shown in Fig. 13. The diameter d_{si} is 0.26 mm for the center post and 0.24 mm for the two lateral posts. l_{cp} is 1.12 mm and l_{in} is 0.31 mm. The IL is less than 0.74 dB across the 85–100-GHz design band and can achieve greater than 60-dB OFF-state isolation.

isolation can be improved. As can be seen from Fig. 14, the addition of a post and the overall increase in the EVA channel length allows greater than 60-dB isolation to be achieved up to 100 GHz. Furthermore, the ON-state response of the device resembles a three-pole bandpass filter—note the additional ripple in the ON-state S_{11} response of Fig. 14 compared to Fig. 13—which vastly increases the 10-dB RL FBW: 19.5% (centered at 92.26 GHz) in the two-pole response is increased to 22.9% (centered at 91.58 GHz) in the three-pole response. The maximum IL in the 85–100-GHz design band is 0.74 dB, a relatively minor engineering trade-off for a significant improvement in isolation.

B. Loss of the Transitions and the SPST Switches

Both SPST switch designs presented in Section IV-A are fed with identical transitions. Since the thru waveguide and the SPST devices are fabricated on the same wafer, the IL obtained from Fig. 12 is assumed to be what is added to the switches fed by the same transitions. Subtracting 0.36 dB from the simulated peak ILs of the two-pole (0.6 dB) and three-pole (0.74) SPST switches, we obtain 0.24 and 0.38 dB for the simulated IL of the respective switching elements.

C. SPDT EVA Switches With E -Plane Bend Transitions

An SPDT switch consists of a common port that is always connected to one of two output branches. Fig. 15 depicts the 3-D model of an SPDT switch with one switching element per branch and two silicon posts per switching element. With power handling in consideration, all corners in the transitions and the device have been rounded with a minimum fillet radius of $50 \mu\text{m}$. The angle (θ) between the two branches has been selected such that the two EVA channels can be placed directly against the transverse width of the common port feed (2.54 mm) and can be computed as follows:

$$\theta = 180^\circ - 2 \sin^{-1} \left(\frac{a}{2W_{EVA}} \right) \quad (17)$$

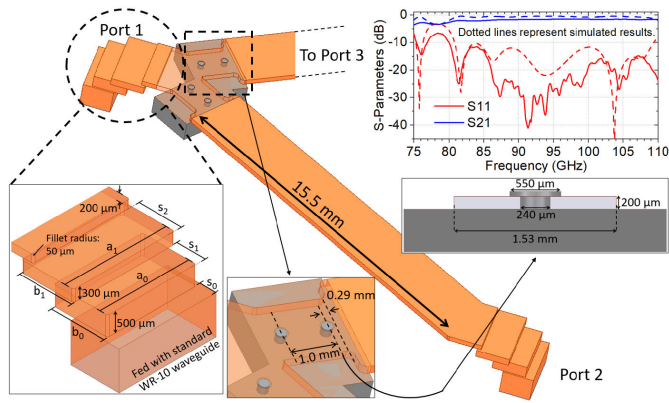


Fig. 15. 3-D model and simulation results of the proposed two-pole photoconductive EVA SPDT switch with E-bend transitions to WR-10 waveguides. Note that the top silicon layer has been rendered transparent to allow visibility inside the structure. The graph shows the simulated and measured data of a 15.0-mm thru line with the E-bend transitions that branch off at the same angle as the proposed switch. The widths of the transition steps a_0 and a_1 are 2.4 and 2.8 mm, respectively, the length of the transition steps b_0 and b_1 are 1.39 and 1.35 mm, respectively, and step offsets s_0 , s_1 , and s_2 are 0.35, 0.74, and 1.2 mm.

where a is the width of the feeding waveguide (2.54 mm) and W_{EVA} is the width of the evanescent channel (1.53 mm) with the resultant angle between the two branches being 67.8° . The diagonal sections on ports 2 and 3 have to be extended to allow for all three required UG-387 connectors to fit on the fabricated device.

In the simulation, port 3 represents the isolated branch, where the silicon posts are photo-excited. The isolation between port 3 and the common port (port 1) is greater than 43.5 dB across the 85–100-GHz design band. Simulation also shows that the signal propagation between the common and through port is no greater than 1.1 dB with an RL at port 1 no less than 15.5 dB across the design band. The measured peak IL of the E-bend transitions with a 15.5-mm thru line is 1.5 dB red compared to the simulated 0.47 dB. Using the same assumptions as in Section IV-B, the simulated IL of the switching element is 0.63 dB.

Likewise, the three-post switch topology presented in Section IV-A can easily be integrated into an SPDT configuration with some minor alterations to its dimensions. Fig. 16 illustrates the 3-D model of the proposed photoconductive three-post SPDT switch. The EVA channel is wider than that of the two-post design and will result in a greater angle of separation between ports 2 and 3 (74.5° , calculated from (11)). The steeper bend angle results in a different input impedance at the ports and therefore the E-bend impedance transformer dimensions from the two-post design cannot be reused in contrast to their SPST counterparts. The measured peak IL of the E-bend transitions for the three-post design with a 15.0-mm thru line is 2.0 dB compared to the simulated 0.37 dB.

Similar to the single throw designs, the three-post SPDT design has significant improvements in isolation over the two-post design, achieving a minimum of 63 dB in the 85–100-GHz design band with a minor trade-off in IL. The maximum through IL in the design band is 1.19 dB, just a 0.09-dB increase over the two-post design. Using the

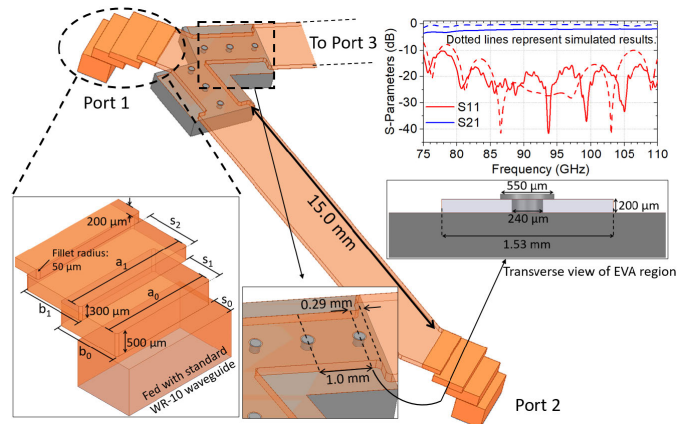


Fig. 16. 3-D model and simulation results of the proposed two-pole photoconductive EVA SPDT switch with E-bend transitions to WR-10 waveguides. The graph shows the simulated and measured data of a 15.5-mm thru line with the E-bend transitions that branch off at the same angle as the proposed switch. The widths of the transition steps a_0 and a_1 are 2.5 and 2.9 mm, respectively, the length of the transition steps b_0 and b_1 are 1.4 and 1.33 mm, respectively, and step offsets s_0 , s_1 , and s_2 are 0.37, 0.72, and 1.11 mm.

same assumptions as in Section IV-B, the simulated IL of the switching element is 0.82 dB.

D. Power Handling Study of SPST Switches

Two of the possible failure modes of operating the SPST switches with high power are as follows: first, there is the possibility of electric breakdown due to the electric field of the mode propagating in the waveguide approaching the limit of the material. In the case of air, it will be approximately 3 MV/m [44]. Second, there is the issue of the $1.2\text{-}\mu\text{m}$ metal films that form the walls of the waveguide channel failing due to high current densities which increase with RF power. It is known from literature that the critical current density of the metals used in the process (gold and copper) is 0.5 MA/cm^2 [42]. Fig. 16 can be converted into a surface current density approximation by taking its product with the skin depth at 85.5 GHz ($0.223\text{ }\mu\text{m}$) which yields 1115 A/m.

According to the field calculator feature in HFSS, the maximum electric field in the structure at 85.5 GHz is 2.599 MV/m which is below the electric breakdown field of air.

A plot of the simulated surface current density (J_{surf}) of the two-post SPST switch is illustrated in Fig. 17. According to the field calculator, the maximum J_{surf} in the structure is located at the discontinuity in the center of the metallic roof of the waveguide where the silicon posts are located. At 5 W of input power, the value of J_{surf} at this location is 1070 A/m which is approaching the theoretical limit of 1115 A/m. In the OFF-state of the device, the electric field and J_{surf} at 5 W was calculated to be 1.287 MV/m and 772.3 A/m, respectively. It can therefore be inferred that the theoretical maximum power handling of this particular structure is approximately 5 W and device failure is most likely to be due to ON-state current.

Likewise, the surface current density plot for the ON-state of the three-post photoconductive switch is shown in Fig. 18. Once again, the maximum J_{surf} can be shown to be at the conductor discontinuity where the silicon posts are etched is

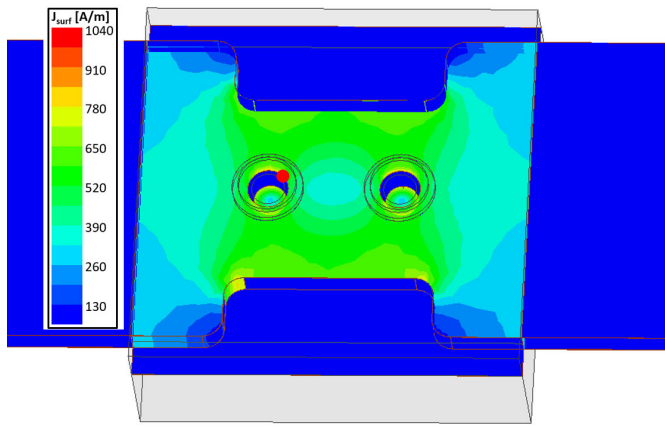


Fig. 17. Simulated surface current plot of the proposed two-post photoconductive SPST switch at 85.5 GHz with 5 W of input RF power for its ON-state. The red sphere marks the spot where the HFSS field calculator calculated the maximum surface current density in the structure to be 1070 A/m.

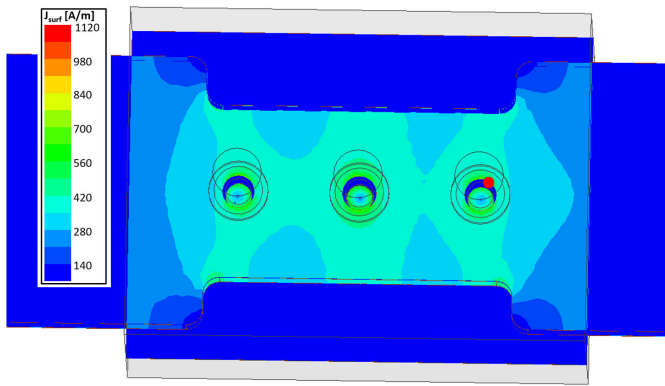


Fig. 18. Simulated surface current plot of the proposed three-post photoconductive SPST switch at 85.5 GHz with 2.9 W of input RF power for its ON-state. The red sphere marks the spot where the HFSS field calculator calculated the maximum surface current density in the structure to be 1097 A/m.

1097 A/m at 2.9 W of input RF power. By contrast, the electric field is 1.529 MV/m which is well below the 3 MV/m. In the OFF-state, the maximum electric field and J_{surf} were calculated to be 0.688 MV/m and 891.8 A/m at 85.5 GHz. Once again, it can be inferred that the theoretical maximum power handling of the proposed three-post switch is approximately 2.9 W with its first failure mode due to ON-state current.

V. ASSEMBLY

Fig. 19(d) shows the assembly and final experimental prototype of a two-pole SPST EVA photoconductive waveguide switch. Alignment is achieved using the dowel pins standard on UG-387/U waveguide flange connectors slotted into the smaller through holes etched using standard silicon deep reactive ion etching (DRIE) processes into both the transition and device wafers, and laser cut into the custom stainless steel flange piece. The details of the microfabrication process can be found in the work reported by Der et al. [31]. Fig. 19(a)–(c) shows the assembly of the switch. The transition wafer is first placed onto the waveguide adapters through the dowel pins located on the adapter flanges. The device wafer is then placed on top of the transition wafer, again using the dowel

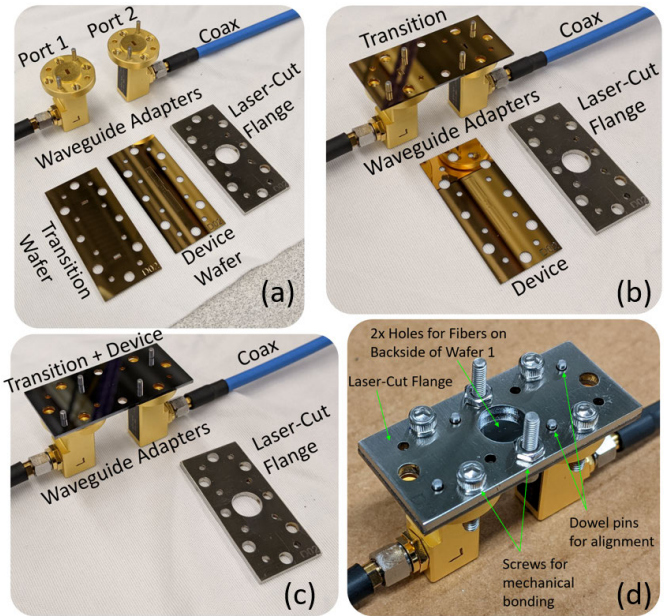


Fig. 19. Pictures of the assembly of the two-pole SPST EVA photoconductive waveguide switch. (a) Picture before assembly, (b) transition wafer placed on the waveguide adapters and aligned using dowel pins, (c) device wafer placed on top of transition wafer, and (d) final assembled two-pole SPST EVA photoconductive waveguide switch.

pins, aligning both wafers to each other and the waveguide openings in the adapters. Finally, the laser-cut metal flange piece is placed on top, and screws are inserted through the larger holes to mechanically bind the wafers together, as shown in Fig. 19(d). The waveguide adapters are primarily used for characterization purposes, and are not part of the switch.

VI. EXPERIMENTAL RESULTS AND ANALYSIS

A. Small-Signal Results of the SPST Switches

The block diagram and photograph of the experimental setup for characterizing the S-parameters of the proposed switches are shown in Fig. 20. Frequency extender modules are used to allow small-signal characterization up to 110 GHz. Fiber optic cables are landed on the chip after the 1.0-mm coaxial to WR-10 adapters are torqued on to the device under test (DUT). The ON-state S-parameters of the two-pole SPST switch (with the laser switched off), and the OFF-state (with the laser switched on), obtained from the vector network analyzer (VNA) are shown in Fig. 21. The device is able to achieve a 10-dB RL bandwidth spanning 82.1–101.3 GHz with a peak ON-state IL of 1.34 dB (at 98.6 GHz) and minimum OFF-state isolation of 40.3 dB.

The experimental setup of the three-pole SPST switch is depicted in Fig. 22. Its measured results plotted in Fig. 23 show that it is able to achieve a peak IL of 1.39 dB (at 94.7 GHz) with at least 57.8 dB OFF-state isolation. The 10-dB RL bandwidth spans 80.4–102.5 GHz.

Since the thru line IL was shown to be around 1.16 dB, we can conclude that the majority of the loss in the aforementioned measurements are from the transitions. The extracted peak IL of the two- and three-pole SPST switches is therefore 0.18 and 0.23 dB, respectively.

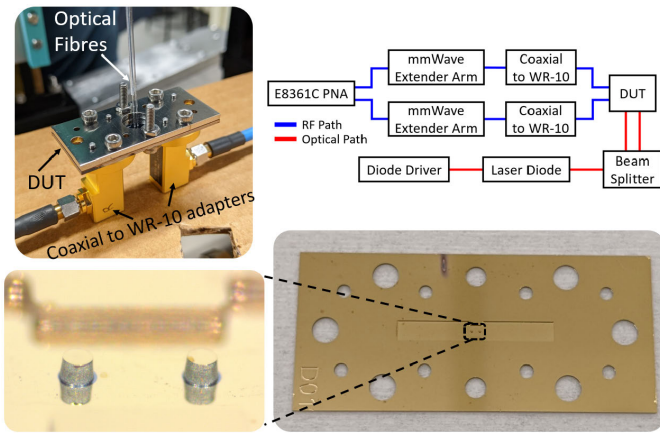


Fig. 20. Block diagram and photographs of the experimental setup for measuring the S-parameters of the proposed two-pole SPST switch. The N5260 extender modules allow for RF characterization up to 110 GHz. An adapter is used to interface the 1.0-mm coaxial output from the extender modules to the WR-10 connectors on the DUT. The optical setup uses a Wavelength Electronics LD5CHA laser diode driver, a 915-nm laser diode from Sheumann Laser Inc., an OZ Optics nonpolarizing beam splitter, and two 400-/440- μm multimode fibers. The size of the switch excluding transitions is 2.54×3.02 mm.

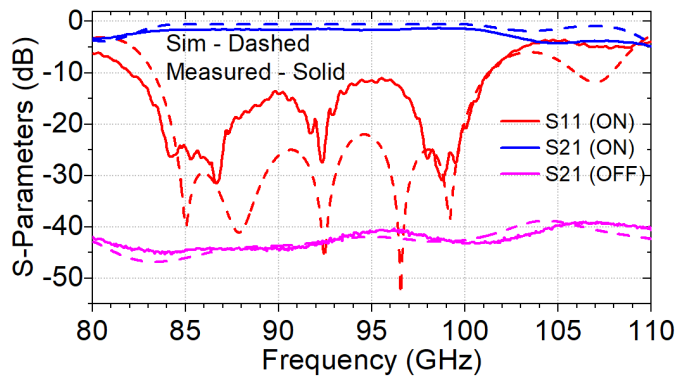


Fig. 21. Measured and simulated results of the proposed two-pole SPST switch for both the thru and isolated states.

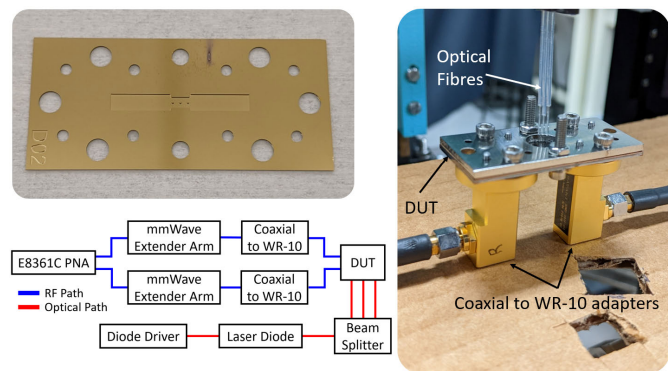


Fig. 22. Experimental setup for the proposed three-pole SPST switch. The size of the switch excluding transitions is 2.54×4.26 mm.

In Figs. 24 and 25, the IL versus frequency at different optical powers are plotted for the two-pole and three-pole SPST switches, respectively. It can be seen from the corresponding group delay plots that the response is relatively flat across the passband of the filter response, and this switch technology can therefore also have applications as tunable attenuators.

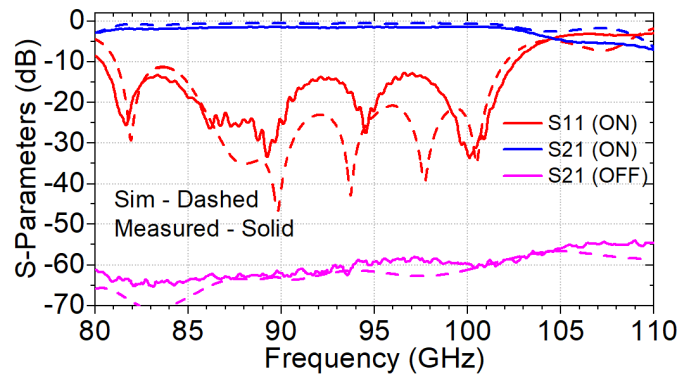


Fig. 23. Measured and simulated results of the proposed three-pole SPST switch for both the thru and isolated states.

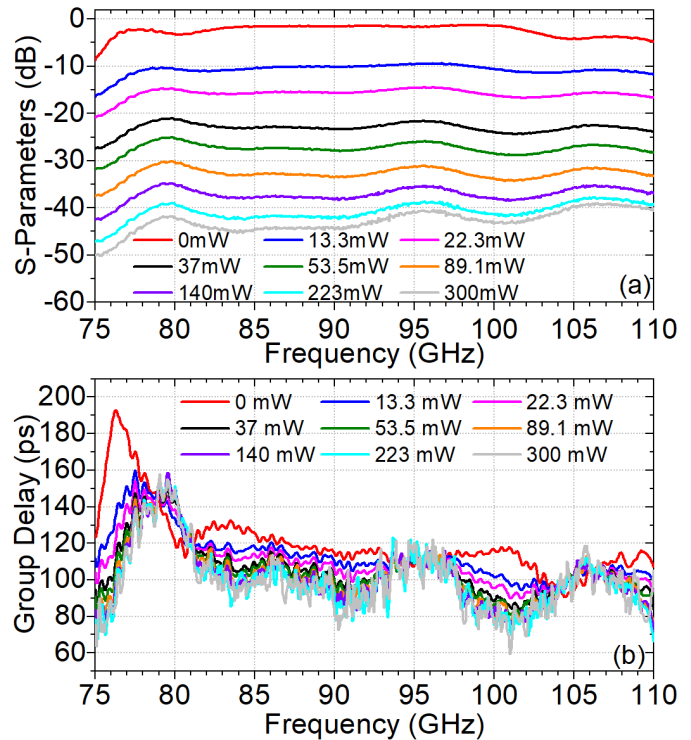


Fig. 24. (a) Measured S_{21} responses at different powers of 915-nm optical excitation for the two-pole SPST switch. (b) Its corresponding group delay response.

A 30-dB isolation can be achieved with just 178 mW of optical power in the two-pole SPST switch. For its three-pole counterpart, this can be achieved with just 111 mW.

B. Small-Signal Results of the SPDT Switches

The experimental setup and microscope images of a two-pole SPDT switch is presented in Fig. 26. The two-pole SPDT switch presented in the original work [31] had silicon posts with an overcut profile. Following adjustments to the process control in refabrication, the new device has a more vertical profile and the lower IL results are presented in Fig. 27. This refabricated device achieved a maximum thru branch IL of 1.66 dB. Since the measured IL of a thru line was around 1.5 dB, it can be concluded that the IL of the switching element itself is 0.16 dB. The design achieved a 22.8% 10-dB RL FBW centered at 95.08 GHz and achieves greater than 40-dB isolation across this operational band.

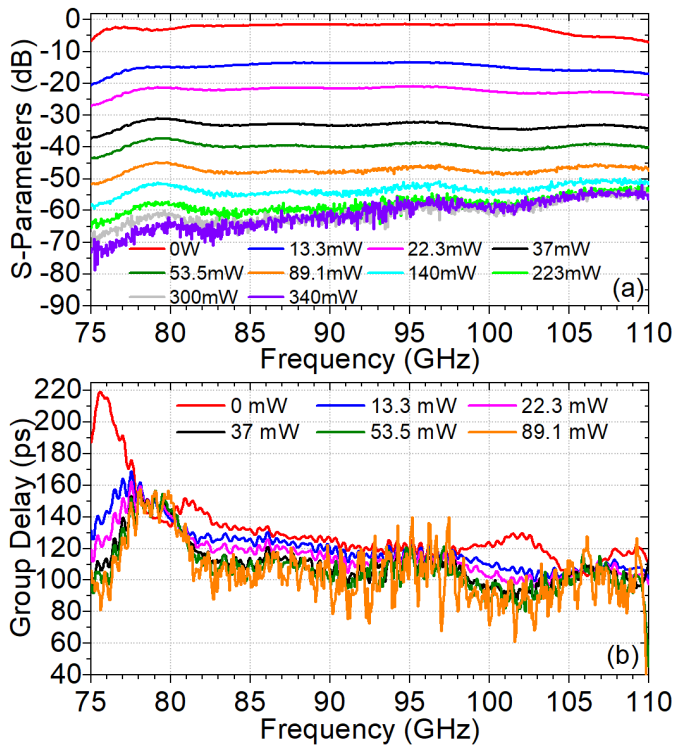


Fig. 25. (a) Measured S_{21} responses at different powers of 915-nm optical excitation for the three-pole SPST switch. (b) Its corresponding group delay response.

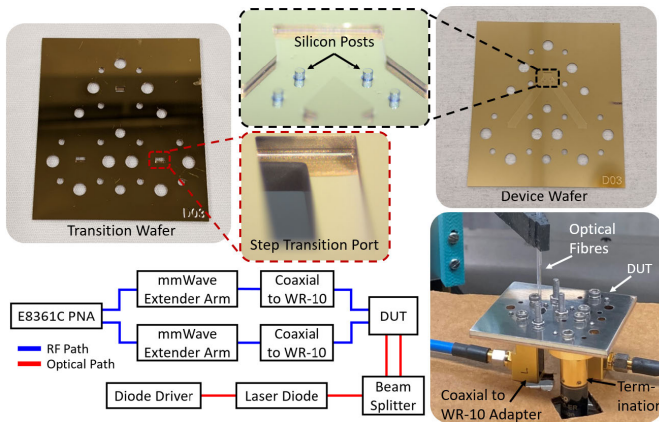


Fig. 26. Assembly and experimental setup of the proposed two-pole SPDT switch.

Likewise, the photograph three-post SPDT switch originally developed in this work is presented in Fig. 28 and it measured S-parameters in Fig. 29. This device has a maximum IL of 2.32 dB. Since the measured IL of its corresponding transition with a thru line is 2.0 dB, it can be concluded that the IL of the switch itself is around 0.32 dB. Furthermore, this device achieved a 10-dB FBW of 21.8% centered at 92.22 GHz and greater than 50-dB isolation from 82.8 GHz and above.

C. Power Handling Measurement of the SPST Switch

The measurement setup depicted in Fig. 30 was used to experimentally evaluate the power handling capabilities of the fabricated SPST switches. A series of amplifiers was used to boost the 85-GHz CW signal from the mmWave

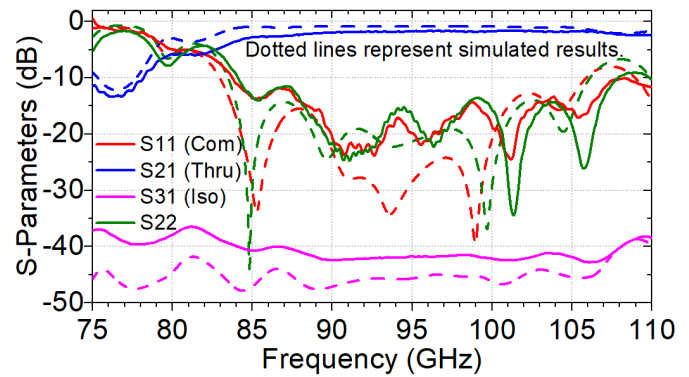


Fig. 27. Measured and simulated results of the proposed two-pole SPDT switch.

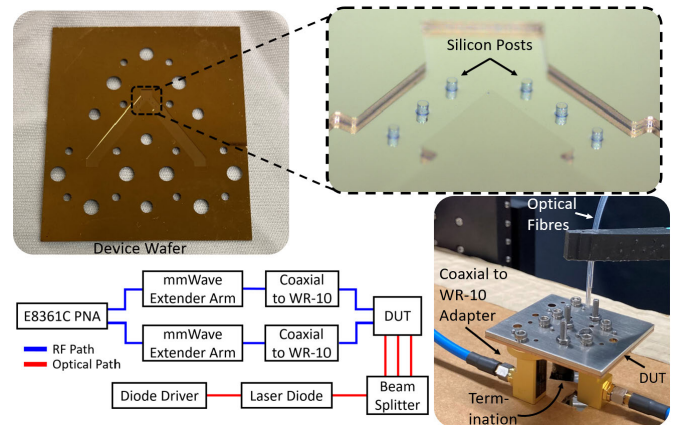


Fig. 28. Experimental setup of the proposed three-pole SPDT switch.

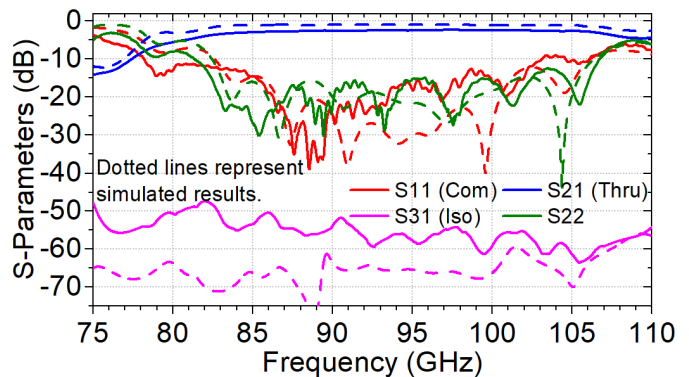


Fig. 29. Measured and simulated results of the proposed three-pole SPDT switch.

module up to +37 dBm (5 W). A variable attenuator dial on the Keysight N5260-60003 mmWave head allowed the input power to be manually tuned. A circulator was placed after the power amplifier to protect it from reflected power in the event that the DUT fails. A power meter configured with a Keysight W8486A sensor was connected to the coupled port of a directional coupler to measure the power going into the DUT. The output of the DUT was then connected to a second directional coupler whose coupled port was fed into port 2 of the VNA. The depicted setup was capable of providing a maximum input power of +32-dBm (1.6-W) CW at 85 GHz at the input of the DUT.

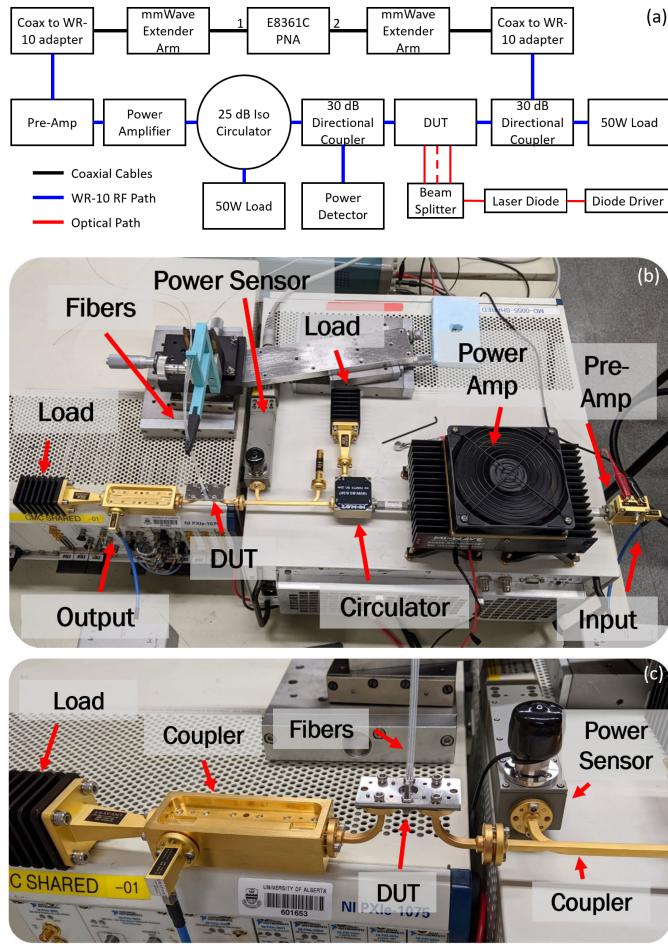


Fig. 30. High power setup. (a) Block diagram for evaluating the power handling capabilities of the fabricated SPST switches. The N5260-60003 has a variable attenuator that can be used to adjust the input power into the power amplifier and by extension, the DUT. A circulator connected to a 50-W termination is used to protect the power amplifier from reflected power should the DUT fail under testing. A power sensor and meter are used to detect and verify the input power into the DUT and a thru-reflect-load (TRL) calibration can be performed to extract the S-parameters of the switch at 85.5 GHz. (b) Photograph of the high power experimental setup. (c) Close-up photograph of the three-pole SPST switch in the high power setup. This setup was able to deliver a maximum of +32 dBm to the DUT.

Both the ON- and OFF-states of the two- and three-pole SPST switches were measured using the setup in Fig. 30. A close-up of the three-pole SPST switch is shown in Fig. 30(c). The switch was subjected to an initial incident power of +20 dBm at 85 GHz and the power was then gradually increased to the +32-dBm CW upper limit of the setup. The S-parameters of the two switches were then measured again at +20-dBm input power, and there were negligible differences to the data plotted in Figs. 21 and 23. This experiment was repeated five times, for both ON-state and OFF-states of the two- and three-pole SPST switches. We can therefore conclude that the switches can handle greater than 1.6 W of RF power. In simulation, it is expected that the two-pole and three-pole SPST switches can handle 5.0 and 2.9 W, respectively, and based on these simulations, the failure mode is expected to be due to the maximum current handling of the metal in the waveguide channel, not the switching element itself. By plating thicker metals in future

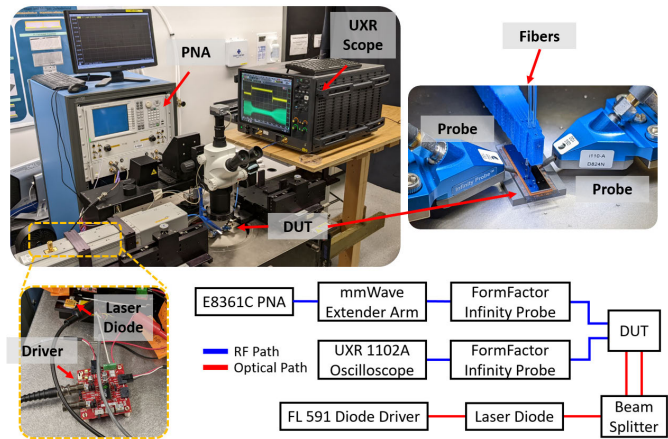


Fig. 31. Block diagram and photographs showing the experimental setup for characterizing the rise and fall times of the silicon photoconductive SPST switch. The E8361C PNA was set to output single frequencies to the optical fiber modulated DUT (SPST switch). The resultant waveform was measured on a Keysight UXR-Series scope.

implementations of this device, the switch is expected to be able to handle even more power.

D. Switching Speed Measurement of the SPST Switch

A block diagram and photographs of the experimental setup for characterizing the switching speed of an SPST switch between 85 and 92.5 GHz are shown in Fig. 31. Due to scheduling considerations at the time, similar light-activated EVA waveguide SPST switches from Jones et al. [30] with CPW to waveguide transitions, operating within the same band were characterized instead. An Agilent E8361C PNA and 110-GHz extender module head was configured to output a single frequency signal to a Cascade Microtech Infinity 110-GHz GSG probe which is landed on the CPW trace of the SPST switch. A second probe was landed on the other side of the device and was connected to a Keysight 110-GHz UXR1102A Infinium UXR-Series oscilloscope. A function generator was configured to output a square wave to modulate the laser diode with a period of 60 μ s which has an internal rise/fall delay of 117.1 ns. A 915-nm ($h\nu = 1.36$ eV, chosen for high quantum efficiency in Si [37]) SP-915-270 Sheamann Laser Inc. laser diode with a pig-tailed 105-/125- μ m single-mode (SM) fiber was connected to an OZ Optics nonpolarizing beam splitter where two of its 400/440 multimode (MM) output fibers are connected to the DUT (the fabricated SPST switch). A 3-D printed structure was used to guide the unterminated fiber ends into backside holes etched above each Si post. A Wavelength Electronics FL591FL laser diode driver was used to drive the laser diode, which has a rise/fall time of 300 ns.

The laser modulated waveforms extracted from the UXR oscilloscope are shown in Fig. 32, displayed in red. The blue waveforms represent the signals from the FL591FL's built-in current monitor pins with a transfer function of 5 mA/mV. Although the diode driver current never fully switches off, the monitor voltage of 50 mV corresponds to 250 mA which is half of the SP-915-270 laser diode's threshold current.

From the extracted waveforms at four measured frequency points, the average 10%–90% rise time and 90%–10% fall time

TABLE I
COMPARISON OF THE PROPOSED THREE-POLE SPDT SWITCH WITH CURRENT STATE-OF-THE-ART SOLUTIONS

Ref.	Technology	Frequency Range (GHz)	10-dB RL FBW (%)	Peak IL (dB)	Isolation (dB)	Power Handling (dBm)	Switching Speed	Volume ^{c,d}
This Work	Photoconductive Si (Waveguide)	82.2–102.3	21.8	0.32	50	32 ^b	4 μ s ^b	53.62
[23]	Photoconductive Si (SIW)	74 – 85.8	15	2.2	30	Unknown	40 μ s	35.5 ^e
[18]	Electromechanical (Waveguide)	75 – 110 ^a	37.8 ^a	0.6 ^a	55 ^a	50	50 ms	> 203
[19]	PIN Diode (Waveguide)	68 – 79 ^a	15 ^a	1.4 ^a	25 ^a	10	50 ns	> 203
[45]	PIN Diode (SIW)	6.76 – 11.8	37	2.1	10	24	2 ns	2.02 ^e

^a Results reported include transition losses.

^b Results extracted from two- and three-pole SPST switches.

^c Excludes the dimensions of biasing circuitry / electromechanical rotors.

^d Normalized to λ^3 in the respective material at the center frequency.

^e Printed circuit board designs, not connectorized with waveguides.

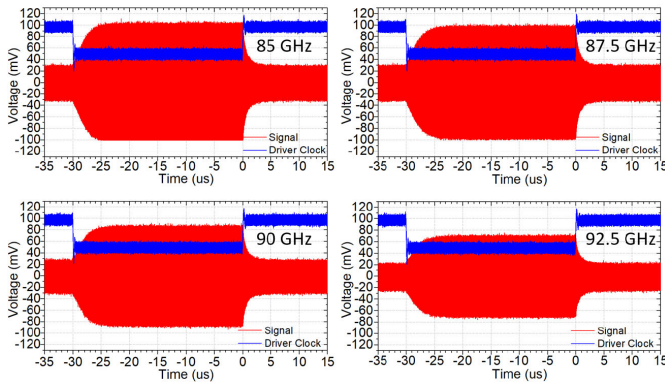


Fig. 32. Time domain waveforms extracted from the Keysight UXR oscilloscope. The E8361C PNA was configured to output single tone waveforms at four different frequencies: 85, 87.5, 90, and 92.5 GHz.

is 3.83 and 1.43 μ s, respectively. The maximum extracted rise and fall time from these measured frequencies are 4.00 and 1.55 μ s, respectively. As can be seen from Table I, these results demonstrate that this technology shows significant promise in being a high-speed alternative to electromechanical RF switches, and lower loss, higher isolation alternative to p-i-n diode switches. The fall time of the switch is dependent on the rate of carrier generation whereas the rise time is dependent on the rate of carrier recombination. Since recombination is generally a slower process, it is expected that the rise time longer than the fall time as is apparent from Fig. 32 [29].

In Table I, the proposed three pole is compared with other waveguide SPDT switches. The proposed design shows the lowest IL compared to other integrated waveguide solutions and has the highest isolation and power handling for solid-state mmWave switches. Furthermore, the proposed device has a vastly superior switching speed compared to electromechanical switches while only sacrificing 10 dB of isolation. Compared with other waveguide connectorized designs, the proposed SPDT switch also offers a significant reduction in device footprint. With improvements to the transition design, the total IL of devices developed using the proposed technology can easily compete with traditionally machined waveguide switches and the device volume can be even further reduced.

VII. CONCLUSION

In summary, this expanded paper of work presented at IMS 2023 further demonstrated the capabilities and promise

of silicon micromachined EVA photoconductive waveguide switches for mmWave technologies. In this expanded work, the design procedure and characterization of a W-Band photoconductive three-pole EVA variable attenuator and SPDT switch were presented which was shown to have significant improvements to the power requirements in achieving high isolation. The fabricated three-pole devices only requires a total CW optical power of 110 mW to achieve a 30-dB isolation, a 38% reduction over a two-pole design. With 900 mW of total optical power, greater than 50 dB of isolation was achieved by the proposed three-pole design from 85 to 100 GHz compared to 40 dB achieved by the two-pole design.

Furthermore, the refabricated two-pole SPDT switch originally presented in [31] was shown to have an extracted IL of 0.2 dB, and its newly presented three-pole counterpart having an extracted IL of 0.32 dB in the W-band.

Additionally, this expanded paper presented the first ever switching speed and power handling characterization of this EVA waveguide switch technology. It was shown that the fabricated switches have a maximum 10%–90% and 90%–10% fall time of 4.00 and 1.55 μ s, respectively. The two-pole and three-pole switching elements have also been shown to be able to handle +32 dBm of CW RF power at 85 GHz in both their ON- and OFF-states.

The results show that silicon-micromachined photoconductive EVA waveguide switches maintain the low IL and high isolation of mmWave electromechanical switch while having a tenfold improvement in switching speed. The proposed switches also demonstrate higher power handling capabilities over mmWave p-i-n diode switches. It is therefore expected that this switch technology will open up new use cases where the performance of mmWave p-i-n diode and electromechanical switches do not meet specifications of 5G and 6G communication devices and mmWave radar applications.

ACKNOWLEDGMENT

The authors would like to thank Keysight Technologies for the loan of a UXR oscilloscope and W8486A power sensor used for characterizing this work. Part of this work was conducted at the University of Alberta nanoFAB Centre. Thomas R. Jones would like to thank Dr. Michael Finot and Dr. Pedro Duarte of RM3 for their help with fabrication of the devices.

REFERENCES

- [1] *3GPP Organizational Partners*, 3GPP, document TS 38.101-1, Valbonne, France, 2017.
- [2] G. Wikström et al., "Challenges and technologies for 6G," in *Proc. 2nd 6G Wireless Summit*, Levi, Finland, Mar. 2020, pp. 1–5.
- [3] H. Viswanathan and P. E. Mogensen, "Communications in the 6G era," *IEEE Access*, vol. 8, pp. 57063–57074, 2020.
- [4] L. U. Khan, I. Yaqoob, M. Imran, Z. Han, and C. S. Hong, "6G wireless systems: A vision, architectural elements, and future directions," *IEEE Access*, vol. 8, pp. 147029–147044, 2020.
- [5] R. F. Holloway, W. H. Weedon, B. Houshmand, and A. Roll, "Next-generation W-band radar testbed," in *Proc. IEEE Radar Conf.*, Waltham, MA, USA, Apr. 2007, pp. 65–71.
- [6] C. Rhoads and D. S. Goshi, "A scalable W-band imaging radar development platform," in *Proc. IEEE Radar Conf.*, Oklahoma City, OK, USA, Apr. 2018, pp. 0344–0348.
- [7] B. Sene, D. Reiter, H. Knapp, H. Li, T. Braun, and N. Pohl, "An automotive D-band FMCW radar sensor based on a SiGe-transceiver MMIC," *IEEE Microw. Wireless Compon. Lett.*, vol. 32, no. 3, pp. 194–197, Mar. 2022.
- [8] D. Kissinger, "D-band and terahertz frontends for 6G wireless communications in SiGe BiCMOS technologies," in *IEEE MTT-S Int. Microw. Symp. Dig.*, vol. 1. Harbin, China, Aug. 2022, pp. 1–3.
- [9] S. A. Busari, S. Mumtaz, S. Al-Rubaye, and J. Rodriguez, "5G millimeter-wave mobile broadband: Performance and challenges," *IEEE Commun. Mag.*, vol. 56, no. 6, pp. 137–143, Jun. 2018.
- [10] D. M. Pozar, *Microwave Engineering*, 4th ed. Hoboken, NJ, USA: Wiley, Nov. 2011.
- [11] P. Harati et al., "E-band downlink wireless data transmission for future satellite communication," in *Proc. Topical Workshop Internet Space (TWIOS)*, Phoenix, AZ, USA, Jan. 2017, pp. 1–4.
- [12] Y. Chen, L. Zhang, Y. He, W. Li, and S.-W. Wong, "A pattern reconfigurable SIW horn antenna realized by PIN diode switches," in *Proc. Comput., Commun. IoT Appl. (ComComAp)*, Shenzhen, China, Nov. 2021, pp. 112–115.
- [13] Y. Gao, M. Khalil, F. Zheng, and T. Kaiser, "Rotman lens based hybrid analog–digital beamforming in massive MIMO systems: Array architectures, beam selection algorithms and experiments," *IEEE Trans. Veh. Technol.*, vol. 66, no. 10, pp. 9134–9148, Oct. 2017.
- [14] E. T. Der, T. R. Jones, and M. Daneshmand, "Miniaturized 4×4 Butler matrix and tunable phase shifter using ridged half-mode substrate integrated waveguide," *IEEE Trans. Microw. Theory Techn.*, vol. 68, no. 8, pp. 3379–3388, Aug. 2020.
- [15] E. T. Der, T. R. Jones, and M. Daneshmand, "A miniaturized 28 GHz 4×4 Butler matrix using shielded ridged half-mode SIW," in *IEEE MTT-S Int. Microw. Symp. Dig.*, Atlanta, GA, USA, Jun. 2021, pp. 776–779.
- [16] Logus Microwave Corporation. *Waveguide Switches*. Accessed: Jul. 27, 2022. [Online]. Available: <https://www.logus.com/products/waveguide-switches/>
- [17] Quinstar Technology Inc. *Electromechanical Waveguide Switches QWZ Series*. Accessed: Jul. 27, 2022. [Online]. Available: <https://quinstar.com/shop/control-products-ferrite/waveguide-pin-switches-single-double-throw/waveguide-pin-switches-double-throw-qss-qsd/>
- [18] Eravant Inc. *Electromechanical Waveguide Switches Control Sub-THz Signals*. Accessed: Jul. 6, 2022. [Online]. Available: <https://sftp.eravant.com/content/resources/Eravant-MWJ-March-2023-SWJ-Switch.pdf>
- [19] Quinstar Technology Inc. *Waveguide PIN Switches—Double Throw QSS/QSD Series*. Accessed: Jul. 27, 2022. [Online]. Available: <https://quinstar.com/shop/control-products-ferrite/waveguide-pin-switches-single-double-throw/waveguide-pin-switches-double-throw-qss-qsd/>
- [20] T. Sickel, P. Meyer, and P. W. van der Walt, "An in situ tunable diode mounting topology for high-power X-band waveguide switches," *IEEE Trans. Microw. Theory Techn.*, vol. 55, no. 2, pp. 281–286, Feb. 2007.
- [21] E. Der, V. Volotovskiy, H. Sun, B. Tomanek, and J. C. Sharp, "Design of a high power PIN-diode controlled switchable RF transmit array for TRASE RF imaging," *Concepts Magn. Reson. B, Magn. Reson. Eng.*, vol. 48B, no. 1, pp. 1–12, Feb. 2018.
- [22] E. Shepeleva, M. Makurin, A. Lukyanov, A. R. Vilenskiy, S. L. Chernyshev, and M. V. Ivashina, "Low-loss K-band photoconductive switches in SIW technology," in *Proc. 50th Eur. Microw. Conf. (EuMC)*, Utrecht, The Netherlands, Jan. 2021, pp. 538–541.
- [23] E. Shepeleva et al., "Integrated W-Band photoconductive switches in SIW technology," *IEEE Microw. Wireless Compon. Lett.*, vol. 31, no. 7, pp. 865–868, Jul. 2021.
- [24] J. Ren, Z. Jiang, P. Fay, J. L. Hesler, C. E. Tong, and L. Liu, "High-performance WR-4.3 optically controlled variable attenuator with 60-dB range," *IEEE Microw. Wireless Compon. Lett.*, vol. 28, no. 6, pp. 512–514, Jun. 2018.
- [25] J. M. González, D. Baillargeat, and L. Roy, "LTCC-based optically tunable microwave filter," in *Proc. CCECE*, Calgary, AB, Canada, May 2010, pp. 1–5.
- [26] A. W. Pang, S. Bensmida, and M. J. Cryan, "Nonlinearity and power handling characterization of an optically reconfigurable microwave switch," in *IEEE MTT-S Int. Microw. Symp. Dig.*, Philadelphia, PA, USA, Jun. 2018, pp. 420–422.
- [27] A. Fisher, Z. V. Missen, T. R. Jones, and D. Peroulis, "A fiber-free DC-7 GHz 35 W integrated semiconductor plasma switch," in *IEEE MTT-S Int. Microw. Symp. Dig.*, Atlanta, GA, USA, Jun. 2021, pp. 27–30.
- [28] E. K. Kowalczyk, C. J. Panagamuwa, and R. D. Seager, "Design and operation influences regarding rise and fall time of a photoconductive microwave switch," in *Proc. Loughborough Antennas Propag. Conf. (LAPC)*, Loughborough, U.K., Nov. 2013, pp. 149–154.
- [29] T. R. Jones, A. Fisher, D. W. Barlage, and D. Peroulis, "A photogenerated silicon plasma waveguide switch and variable attenuator for millimeter-wave applications," *IEEE Trans. Microw. Theory Techn.*, vol. 69, no. 12, pp. 5393–5403, Dec. 2021.
- [30] T. R. Jones, A. Fisher, D. W. Barlage, and D. Peroulis, "A W-band photoconductive evanescent-mode waveguide switch," in *IEEE MTT-S Int. Microw. Symp. Dig.*, Denver, CO, USA, Jun. 2022, pp. 959–962.
- [31] E. T. Der et al., "A W-band SPDT photoconductive evanescent-mode waveguide switch," *IEEE Microw. Wireless Technol. Lett.*, vol. 33, no. 6, pp. 831–834, Jun. 2023.
- [32] A. Fisher, T. R. Jones, and D. Peroulis, "A DC to 110 GHz plasma switch," in *IEEE MTT-S Int. Microw. Symp. Dig.*, Denver, CO, USA, Jun. 2022, pp. 251–254.
- [33] A. Fisher, T. R. Jones, and D. Peroulis, "A reconfigurable reflective/absorptive SPDT plasma switch," in *IEEE MTT-S Int. Microw. Symp. Dig.*, San Diego, CA, USA, Jun. 2023, pp. 1065–1068.
- [34] A. Fisher, T. R. Jones, and D. Peroulis, "Design and optimization of a high-power solid-state plasma RF switch," *IEEE Trans. Microw. Theory Techn.*, early access, Aug. 1, 2023, doi: [10.1109/TMTT.2023.3297365](https://doi.org/10.1109/TMTT.2023.3297365).
- [35] J. O. García, J. C. M. Lernas, V. E. Boria, and M. Guglielmi, "On the integration of microwave filters and waveguide switches," *IEEE Microw. Wireless Compon. Lett.*, vol. 31, no. 3, pp. 265–268, Mar. 2021.
- [36] X. Zhao, O. Glubokov, and J. Oberhammer, "A silicon-micromachined waveguide platform with axial ports for integrated sub-THz filters," *IEEE Trans. Microw. Theory Techn.*, vol. 70, no. 2, pp. 1221–1232, Feb. 2022.
- [37] S. Sze and K. K. Ng, *Physics of Semiconductor Devices*. Hoboken, NJ, USA: Wiley, Oct. 2006.
- [38] C. Hu, *Modern Semiconductor Devices for Integrated Circuits*. Upper Saddle River, NJ, USA: Prentice-Hall, Mar. 2009.
- [39] G. F. Craven and C. K. Mok, "The design of evanescent mode waveguide bandpass filters for a prescribed insertion loss characteristic," *IEEE Trans. Microw. Theory Techn.*, vol. MTT-19, no. 3, pp. 295–308, Mar. 1971.
- [40] P. Ludlow, V. Fusco, G. Goussetis, and D. E. Zelenchuk, "Applying band-pass filter techniques to the design of small-aperture evanescent-mode waveguide antennas," *IEEE Trans. Antennas Propag.*, vol. 61, no. 1, pp. 134–142, Jan. 2013.
- [41] J.-S. Hong and M. J. Lancaster, *Microstrip Filters for RF/Microwave*, 2nd ed. Hoboken, NJ, USA: Wiley, Mar. 2011.
- [42] G. M. Rebeiz, *RF MEMS: Theory, Design, and Technology*. Hoboken, NJ, USA: Wiley, Feb. 2003.
- [43] R. J. Cameron, C. M. Kudsia, and R. R. Mansour, *Microwave Filters for Communication Systems*. Hoboken, NJ, USA: Wiley, Mar. 2018.
- [44] M. G. Hogg, I. V. Timoshkin, S. J. MacGregor, M. P. Wilson, M. J. Given, and T. Wang, "Electrical breakdown of short non-uniform air gaps," in *Proc. 19th IEEE Pulsed Power Conf. (PPC)*, San Francisco, CA, USA, Jun. 2013, pp. 1–4.
- [45] I. Lim and S. Lim, "Substrate-integrated-waveguide (SIW) single-pole-double-throw (SPDT) switch for X-band applications," *IEEE Microw. Wireless Compon. Lett.*, vol. 24, no. 8, pp. 536–538, Aug. 2014.

Eric T. Der (Graduate Student Member, IEEE) received the B.Sc. degree in electrical engineering (cooperative program) from the University of Alberta, Edmonton, AB, Canada, in 2017, where he is currently pursuing the Ph.D. degree in electrical engineering under the supervision of Prof. Kambiz Moez.

His primary research interests include the development of miniaturized integrated waveguide beamforming networks and components for 5G and 6G communication systems.

Mr. Der has been serving as an Executive in the award winning IEEE Northern Canada Section AP-S/MTT-S Joint Chapter since 2020.



Thomas R. Jones (Member, IEEE) received the B.Sc. and Ph.D. degrees in electrical and computer engineering from the University of Alberta, Edmonton, AB, Canada, in 2007 and 2019, respectively.

From 2008 to 2013, he was a Project Engineer at Tracer Industries Canada Ltd., Edmonton. In 2013, he joined the Microwave to Millimeter-wave (M2M) Group, University of Alberta, as a Research Assistant. From 2019 to 2021, he was a Visiting NSERC Post-Doctoral Fellow with Purdue University, West

Lafayette, IN, USA, and a Post-Doctoral Fellow with the University of Alberta. He is currently a Senior Research Associate with Purdue University. His research interests include microwave, millimeter-wave, and sub-THz design for high-speed and high-power communication systems and radar, reconfigurable RF front ends and tunable filters, and the microfabrication of on-chip millimeter-wave devices.

Dr. Jones is a recipient of the Queen Elizabeth II Graduate Scholarship, the Alberta Innovates Technology Futures (AITF) Graduate Student Scholarship, the Natural Science and Engineering Research Council (NSERC) Alexander Graham Bell Canada Graduate Scholarship, and the NSERC Postdoctoral Fellowship. He was a recipient of the First Place Excellence in Nanofabrication Award at the 2017 CMC TEXPO Student Design Competition held in Montreal. He has also served as the Finance Chair for the IEEE 2019 Canadian Conference on Electrical and Computer Engineering and served in various roles, including the Vice-Chair for the award-winning IEEE Northern Canada Section AP-S/MTT-S Joint Chapter. He is currently serving as the IEEE MTT-S MGA Regional Coordinator for R7 Canada.



Alden Fisher (Member, IEEE) received the B.S. degree (Hons.) in electrical engineering from Purdue University, West Lafayette, IN, USA, in 2017, where he is currently pursuing the Ph.D. degree under the supervision of Prof. Dimitrios Peroulis.

His current research interests include solid-state plasma devices and their role in reconfigurable, high-frequency, and high-power RF electronics. He has also explored wireless energy transfer.

Mr. Fisher is a member of Eta Kappa Nu. He received the First Place in the Packaged C-Band

Filter (MTT-5 and MTT-16) Student Design Competition at IMS 2022 and is a recipient of the 2023 MTT-S Graduate Fellowship. He was the Local IEEE MTT-S Chapter Chair.



Kambiz Moez (Senior Member, IEEE) received the B.Sc. degree in electrical engineering from the University of Tehran, Tehran, Iran, in 1999, and the M.Sc. and Ph.D. degrees from the University of Waterloo, Waterloo, ON, Canada, in 2002 and 2006, respectively.

Since January 2007, he has been with the Department of Electrical and Computer Engineering, University of Alberta, Edmonton, AB, Canada, where he is currently a Full Professor and the Director of the Electrical Engineering Program. His

research interests include the analysis and design of analog, radio frequency, and millimeter-wave CMOS integrated circuits and systems for a variety of applications, including wired/wireless communications, biomedical imaging, instrumentations, radars, and power electronics.

Dr. Moez is a Registered Professional Engineer in the province of Alberta. He is currently serving as an Associate Editor for the IEEE TRANSACTIONS ON CIRCUITS AND SYSTEMS I: REGULAR PAPERS and *IET Electronics Letters*.

Douglas W. Barlage, photograph and biography not available at the time of publication.



Dimitrios Peroulis (Fellow, IEEE) received the Ph.D. degree in electrical engineering from the University of Michigan, Ann Arbor, MI, USA, in 2003.

From 2019 to 2023, he served as the Michael and Katherine Birck Head of ECE and a Special Adviser to the Dean of Engineering on online learning. He is currently the Senior Vice President for Purdue University Online and the Reilly Professor with the Elmore Family School of Electrical and Computer Engineering, Purdue University, West Lafayette, IN, USA. He has coauthored over 450 journal articles

and conference papers. His research interests include reconfigurable systems, plasma RF electronics, and RF-assisted lyophilization. He has been a Key Contributor in developing high-quality widely tunable filters and novel filter architectures based on miniaturized high- Q cavity-based resonators.

Dr. Peroulis received the National Science Foundation CAREER Award in 2008. In 2019, he received the "Tatsuo Itoh" Award and in 2014, he received the Outstanding Young Engineer Award both from the IEEE Microwave Theory and Techniques Society (MTT-S). In 2012, he received the Outstanding Paper Award from the IEEE Ultrasonics, Ferroelectrics, and Frequency Control Society (Ferroelectrics Section). His students have received numerous student paper awards and other student research-based scholarships. He has been a Purdue University Faculty Scholar and has also received 11 teaching awards, including the 2010 HKN C. Holmes MacDonald Outstanding Teaching Award and the 2010 Charles B. Murphy Award, which is Purdue University's highest undergraduate teaching honor.